Mineral precipitation and geometry alteration in porous structures: How to upscale variations in permeability-porosity relationship?

Mohammad Masoudi[1, *], Mohammad Nooraiepour[1], Hang Deng[2] and Helge Hellevang[1]

[1] Department of Geosciences, University of Oslo, P.O. Box 1047 Blindern, 0316 Oslo, Norway
[2] College of Engineering, Peking University, Beijing, China, 100871
* Correspondence: mohammad.masoudi@geo.uio.no

Mineral precipitation and geometry alteration in porous structures: How to upscale variations in permeability-porosity relationship?

Mohammad Masoudi[1], Mohammad Nooraiepour[1], Hang Deng[2] and Helge Hellevang[1]

[1] Department of Geosciences, University of Oslo, P.O. Box 1047 Blindern, 0316 Oslo, Norway

[2] College of Engineering, Peking University, Beijing, China, 100871

* Correspondence: mohammad.masoudi@geo.uio.no

Abstract

Porous materials in natural and engineered environments are subject to morphological changes resulting from interacting chemical and physical processes. The complexity of coupled flow, transport, and chemical processes that occur on different temporal and spatial scales makes it difficult to predict the resulting porosity and permeability alterations. Delineating the controls of mineral precipitation reactions is particularly challenging because it requires the implementation of nucleation criteria and precipitation attributes. By conducting pore-scale simulations, we studied how the amount and stochastic distribution of crystallites, controlled by nucleation, affect the pore geometry and permeability in two-dimensional porous structures. The observed relationships between porosity and permeability show characteristics that differ from ones that are typically applicable in dissolving porous media because of the clogging effect. Additionally, we propose a stochastic framework that upscales the co-evolution of permeability and porosity across length scales. This framework enables precise communication of clogging behavior to continuum-scale simulations based on statistical probability distributions of permeability-porosity variations.

Keywords: Upscaling; Probabilistic nucleation; Mineral precipitation; Geometry evolution; Permeability-Porosity; Reactive transport; Porous media

Plain language summary

Precipitation of minerals inside the porous materials changes their internal structure and how the fluids can move through them. We used a special computer model that can explicitly capture the porous media's structure to study this phenomenon. Our research revealed that the way minerals are distributed and the initial shape of the porous material play a crucial role in these structural changes. When dealing with large-scale problems, we face limitations in computational resources, preventing us from using detailed computer codes. As a solution, we rely on average measurements and transfer information from small-scale simulations to larger ones. Two important averages we use are “porosity” (the percentage of void space in the materials) and “permeability” (how easily fluids flow). Typically, a simple formula like a power-law is used to relate them. In this work, we found that different processes change porous materials in different ways. So, instead of just one formula, we suggest using a range of statistical parameters. We also suggest a step-by-step method to transfer details from small-scale to large-scale simulations.

1 Introduction

Many natural and engineered systems and coupled processes have been typically modeled by reactive transport models (RTM) at the continuum scale. With the continuum assumption, averaged properties are assigned in each grid cell. The averaged values are often estimated, i.e., upscaled from the smaller scale features. Upscaling can be achieved by mathematically deriving macroscale equations from microscale principles[1], or by developing constitutive relations from finer scale simulations and experiments.

Porosity and permeability are two of the most important and common continuum scale parameters in hydrological and hydrogeochemical modeling. Porosity provides a homogenized representation of the pore structures, and permeability is usually upscaled based on permeability–porosity relations. These relations do not explicitly capture the pore-scale complexities and micro-scale features, and only provide approximations at the continuum scale. Establishing a relationship between porosity and permeability in porous media to preserve as much as pore-scale dynamics is an increasingly important area of research, particularly with recent advancements in computation and imaging technologies. Research to establish a correlation between porosity and permeability can be broadly categorized into two groups. The first category relates the permeability of an intact medium to its porosity, commonly found in the field of digital rock physics[2–6]. The second category focuses on linking changes in permeability to alterations in porosity, i.e., the investigation of permeability evolution[7–10] that can be caused by a range of coupled thermal, hydraulic, mechanical, and chemical (THMC) processes. Despite their similar goals, these two categories are fundamentally different. Still, porosity-permeability relations developed from these two types of studies are mostly used interchangeably. This paper focuses on the changes in permeability and porosity and their relationship in porous media.

The morphology changes of porous materials (e.g., fractured geomaterials, fuel cell, and brain tissues) are influenced by interacting chemical-physical processes such as dissolution, precipitation, biomass accumulation, swelling, shrinking, and mechanical compaction. The intimate interplay between different factors affects permeability changes. For instance, during dissolution and precipitation, different reactive regimes characterized by Peclet (Pe) and Damkohler (Da) numbers affect the relationships between porosity and permeability [11–13]. In turn, anisotropic rock texture and preferential flow paths can also significantly impact dissolution-precipitation patterns [14–17].

Specifically, the precipitation of secondary phases during reactive transport is a complex phenomenon in various geological and environmental settings. Substances such as hydrate[18], asphaltene[19,20], biomass[7], and minerals[21–24] can deposit in porous media and clog pore spaces differently. Among these substances, minerals have an added level of complexity because of nucleation, the pre-growth phenomenon that determines the starting time and location of mineral growth. Studying mineral precipitation in natural and engineered porous materials has broad implications for addressing several United Nations' Sustainable Development Goals, including clean water and sanitation, climate action, and affordable and clean energy. Mineral precipitation can significantly influence the behavior of contaminants in the environment by altering their solubility and mobility, thereby affecting their transport and fate. The sequestration of inorganic pollutants (such as arsenic, antimony, selenium, and other heavy and toxic metals) in carbonates [25–29] and

retention of radium by its co-precipitation with barium sulfate to treat contaminated water, water waste and industrial waste [30–32] are only a few examples. Mineral precipitation in porous rocks plays a vital role in addressing several geoenergy challenges [33], such as scale formation in geothermal systems [34], injectivity impairment due to salt aggregates during CO_2 storage [24,35,36], and clogging of reservoir rocks during enhanced hydrocarbon recovery. Favorable effects of mineral precipitation include CO_2 mineral trapping in basalt [37] and fracture healing of caprock leakage pathways in storage sites [23].

Essentially, mineral nucleation is a critical factor in controlling the distribution of minerals over time and space [9,22,38–43]. The interplay between solute transport, nucleation, growth, and porous media structure is intricate. Several experimental and numerical works have shown that the same amount of porosity reduction due to mineral precipitation might result in different permeability reductions [9,14,49–51,16,22,39,44–48]. Furthermore, arbitrary selection of clogging models in RTMs may lead to considerable errors in predicted permeability for the same amount of porosity loss [7,52]. Despite all the mentioned variations and uncertainties, the permeability–porosity evolution during RTM in the continuum scale is usually oversimplified and handled with a single equation with a constant variable. Therefore, a process-based approach is necessary when analyzing permeability-porosity evolution.

In this work, we study the effect of crystallite distribution (controlled by nucleation) on pore geometry alteration and, consequently, permeability evolution in diverse two-dimensional porous media. In addition, for the first time, we propose a framework for upscaling the co-evolution of permeability-porosity, which combines simulations at both the pore and continuum scales to produce a more accurate representation of permeability changes in porous media. This study enables a comprehensive delineation of the clogging behavior in porous media, which can inform decision-making in various applications, such as CO_2 storage, water treatment, and geo-energy resources.

2 Materials and Methods

2.1 Selection of porous geometries

Six different two-dimensional (2D) porous geometries were generated using PoreSpy[53] (Fig. 1) to perform pore-scale reactive transport modeling (RTM). The synthetic porous media structures encompass (a) highly heterogeneous structures that mimic natural rock geometries with different permeability and anisotropies (Fig. 1, top row) and (b) simplified homogeneous geometries with ordered and disordered arrangement of spheres (Fig. 1, bottom row). The pore volume (porosity) for all cases is chosen to be approximately 60% (59.6%-60.7%) because the percolation thresholds of 2D square lattice with site percolation is found to be 59.27% [54]. The initial permeability of the structures varies from 1.57e-10 to 2.59e-9 m^2. In the text, we refer to each geometry in Figure 1 as Het (heterogeneous, top row) or Hom (homogeneous, bottom row), followed by their number. For instance, Het_2 for heterogeneous medium number 2. The properties of the structures are summarized in Table S-1.

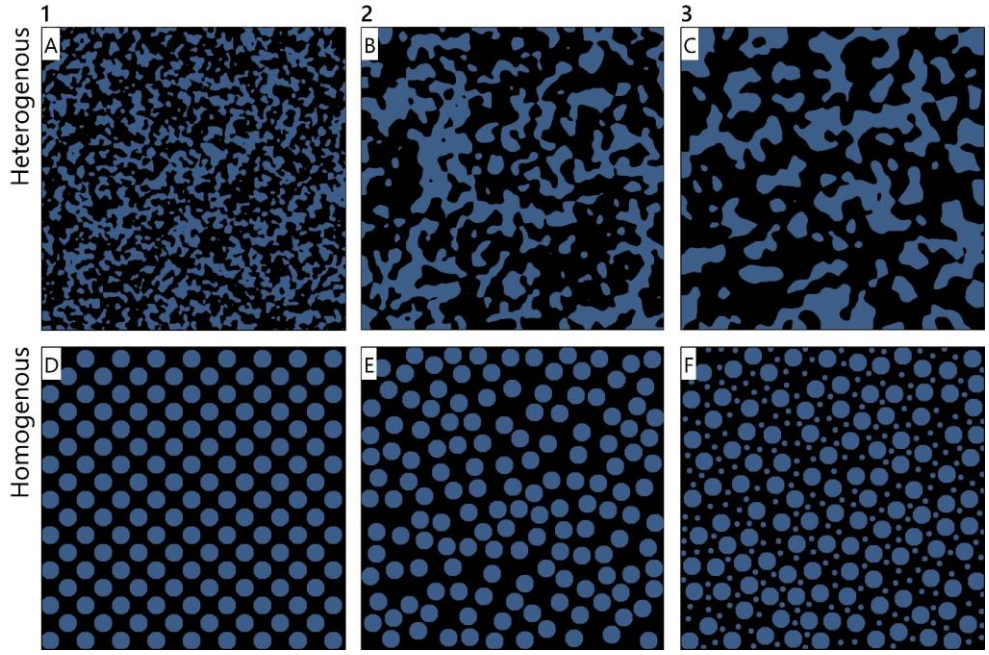

Figure 1: The selection of random two-dimensional porous geometries, representing natural rock geometries (top row, heterogeneous) and simplified ordered/disordered porous structures (bottom row, homogeneous). The darker (black) and lighter (blue) colors represent pore space and grains (solid phases).

2.2 Model and assumptions

We used the Lattice Boltzmann Method (LBM) for RTM and flow simulations with the D2Q9 lattice scheme. The advection-diffusion-reaction equation was used for tracking the concentration of different species:

$$\frac{\partial C_j}{\partial t} + \nabla.\left(-D_j \nabla C_j + uC_j\right) = R_j \quad (1)$$

Where C_j [NL^{-3}] is the aqueous concentration of species j, D_j [L^2T^{-1}] is the diffusion coefficient of species j in water, u is velocity [LT^{-1}], and R_j [$NL^{-3}T^{-1}$] is the source or sink term due to reactions for species j. The discretized LB equation used to solve the ADR equation (the mass transport) is as follows:

$$g_i^j(x + c_i\Delta t, t + \Delta t) = g_i^j(x,t) - \frac{\Delta t}{\tau_g}\left[g_i^j(x,t) - g_i^{eq,j}(x,t)\right] + \Delta t Q_i^j(x,t) \quad (2)$$

$$g_i^{eq,j} = w_i C^j \left(1 + \frac{c_i.u}{c_s^2}\right) \quad (3)$$

In which g_i^j is discrete distribution function, $g_i^{eq,j}$ is equilibrium distribution function, and C^j is concentration of species j. Δt is time resolutions, τ_g is relaxation time, c_s is lattice speed of sound, and c_i and w_i are discrete velocity sets and weighting coefficients.

The D2Q9 lattice scheme used, where 2 is the number of spatial dimensions (x and y) and 9 is the number of discrete velocities, w_0 = 4/9, $w_{1\text{-}4}$ = 1/9, and $w_{5\text{-}8}$ = 1/36 and

$$c_i = \begin{cases} (0,0), i = 0 \\ (\cos\theta_i, \sin\theta_i), \theta_i = (i-9)\frac{\pi}{2}, i = 1-4 \\ (\cos\theta_i, \sin\theta_i)\sqrt{2}, \theta_i = (2i-9)\frac{\pi}{4}, i = 5-8 \end{cases} \quad (4)$$

After solving Equation 2, the concentration of species j is calculated as follows:

$$C^j = \sum_{i=0}^{8} g_i^j \quad (5)$$

The source/sink term is given by:

$$Q_i^j(x,t) = w_i\left[q_N^j(x,t) + q_G^j(x,t) + q_S^j(x,t)\right] \quad (6)$$

$$q_N^j = \frac{dC_N^j}{\Delta t} \quad (7)$$

$$q_G^j = \frac{dC_G^j}{\Delta t} \quad (8)$$

$$q_S^j = D_j(SR^0 - SR), if\ SR < SR^0 \quad (9)$$

The subscripts N, G, and S in Equation (6) denote the nucleation, growth, and infinite source of the solution on top of the substrate. The simple reaction of $\{A_{(aq)} \rightleftarrows A_{(s)}\}$ is considered:

$$R_G = k_G S(1 - \mathrm{SR}) \quad (10)$$

where R_G [mol·s^{-1}] is the growth or reaction rate, k_G [mol·m^{-2}·s^{-1}] is the growth rate constant, S [m^2] is the reactive surface area, and SR is the saturation ratio:

$$SR = \frac{C_A}{C_{eq}} \quad (11)$$

where, C_A [mol·L^{-1}] is the concentration of mineral A in the aqueous phase, and C_{eq} [mol·L^{-1}] is the equilibrium aqueous concentration of mineral A.

The simulation domain was a quasi-2D system of 500×500×1 grid cells with a spatial resolution of 20 μm. The periodic boundary condition was applied for all the boundaries. The domain was initially water saturated. There is no advection in the system, and an infinite source of the oversaturated solution was imposed on top of the domain via a source term in the discretized Lattice Boltzmann (LB) equation. More details of the LBM model, mineral growth (reaction) model, and subgrid assumptions and implementations can be found in our previous works [9,39,42,43,55].

This work did not use the entire nucleation model criteria. Instead, a pre-defined number of crystallites (as a proxy for stable nucleation sites) were populated randomly for initializing the system, as the main focus is tracking and quantifying consequences of mineral precipitation on the hydrodynamics of porous media. Each pore lattice was assumed to be on a homogeneous nonreactive solid substrate surface, as schematically depicted in Figure S1 (Supplementary Information). The crystallites may form everywhere within the entire pore space, but each grid cell can only have one crystallite. This is equivalent of only considering heterogeneous nucleation events (nucleation at the solid-liquid interface). The reaction rate afterward controlled the continued growth of the introduced crystallites until reaching the clogging state. Three crystallization cases (10, 100, and 1000 crystallite) with eight stochastic realizations were simulated for each porous media

geometry. Crystallites have the same size (1e-9 radios). Growth rates were the same for all crystals (1.5488e-06 mol·m^{-2}·s^{-1}).

The permeability of the evolving domains was calculated using LBM for hydrodynamics. We used Yantra open source code [56] to calculate the velocity fields at the x and y directions. Periodic and no flow boundary conditions were applied to the boundaries along and perpendicular to the flow direction, respectively. To recover the hydrodynamic properties in single-phase fluid flow, continuity equation (Equation 12) and Navier-Stokes equation (Equation 13) should be solved simultaneously. To do so, the LB model in equation 14 was used.

$$\nabla . u = 0 \tag{12}$$

$$\rho \frac{\partial u}{\partial t} + \rho u . \nabla u = -\nabla P + \mu \nabla^2 u + F \tag{13}$$

where ρ [ML^{-3}] is density, u [LT^{-1}] is velocity, P [M^{1}L^{-1}T^{-2}] is pressure, μ [M^{1}L^{-1}T^{-1}] is dynamic viscosity and F [M^{1}L^{-2}T^{-2}] is body force.

$$f_i(x + c_i \Delta t, t + \Delta t) = f_i(x,t) - \frac{\Delta t}{\tau}\left(f_i(x,t) - f_i^{eq}(x,t)\right) + (1 - \frac{\Delta t}{2\tau})F_i(x,t) \tag{14}$$

$$f_i^{eq} = w_i \rho \left(1 + \frac{u . c_i}{c_s^2} + \frac{(u . c_i)^2}{2c_s^4} - \frac{u . u}{2c_s^2}\right) \tag{15}$$

$$F_i = w_i \left(\frac{c_i . F_\alpha}{c_s^2}\right) \tag{16}$$

$$c_s^2 = \frac{1}{3}\left(\frac{\Delta x}{\Delta t}\right)^2 \tag{17}$$

where Δt and Δx are time and space resolutions. f_i is discrete distribution function, f_i^{eq} is equilibrium distribution function for hydrodynamics. F_i is body force, c_s is lattice speed of sound, u is velocity, ρ is density, and τ is relaxation time for hydrodynamics. It should be noted that the lattice speed of sound, c_s, can vary based on the chosen lattice structure. Because we used the same lattice structure (D2Q9), weighting coefficients (w_i), and discrete velocity sets (c_i) for ADR LB and hydrodynamics LB, the lattice speed of sound in Equation 17 can be used for both Equation 3 and Equation 15. After solving Equation 14, density and velocity can be calculated from the following equations:

$$\rho = \sum_{i=0}^{18} f_i^j \tag{18}$$

$$u = \frac{1}{\rho} \sum_i f_i \, c_i + \frac{F_\alpha}{2\rho} \tag{19}$$

Darcy's law was used to calculate the permeability of the porous media:

$$\bar{J} = -\frac{k}{\mu} \nabla P \tag{20}$$

Where $\bar{J}$ [LT^{-1}] is average flux (flow rate per unit area), k [L^2] is permeability, μ [M^{1}L^{-1}T^{-1}] is dynamic viscosity, and ∇P [M^{1}L^{-1}T^{-2}] is pressure gradient. ∇P in equation 20 can be replaced by F, the body force, in equation 13.

3 Results and Discussion

Figure 2 compares the normalized permeability-porosity relationships (k/k_0 plotted against φ/φ_0) from six different porous geometries, and three crystallization cases (10, 100, and 1000 crystallites) with power-law formulations with different exponents ($k/k_0 = (\phi/\phi_0)^n$). Overall, pore morphological alteration from mineral precipitation and growth affected heterogeneous geometries (representing real rock structures) more substantially than homogeneous structures. The difference between different numbers of precipitated crystallites is more distinct for homogeneous systems, even at early times (Fig. 2). The degree of permeability impairment increases as the number of crystals increases. However, the scatter of data points decreases as the number of crystals increases. Put differently, stochastic realizations of 10 crystallites account for a large portion of the variations in contrast to 10^3 crystallite cases that are fairly concentrated on a small part (Figs. 2C-E). The separation between heterogeneous and homogeneous geometries is more evident for 10 and 10^2 cases. The data points for 10s lie between n=2-16, for 10^2s, n=4-16, and for 10^3s, n=10-16 (Figs. 2C-E).

The complete simulation results for each case are shown in Figures S2 and S3, where each curve represents one single simulation with the initial position of crystallites varied randomly. Changes in permeability because of mineral precipitation and geometrical evolution are investigated as a function of (a) total porosity changes (expressed as φ/φ_0) in Figures 2, 3, and S2, and (b) reaction progress (ξ) in Figure S3.

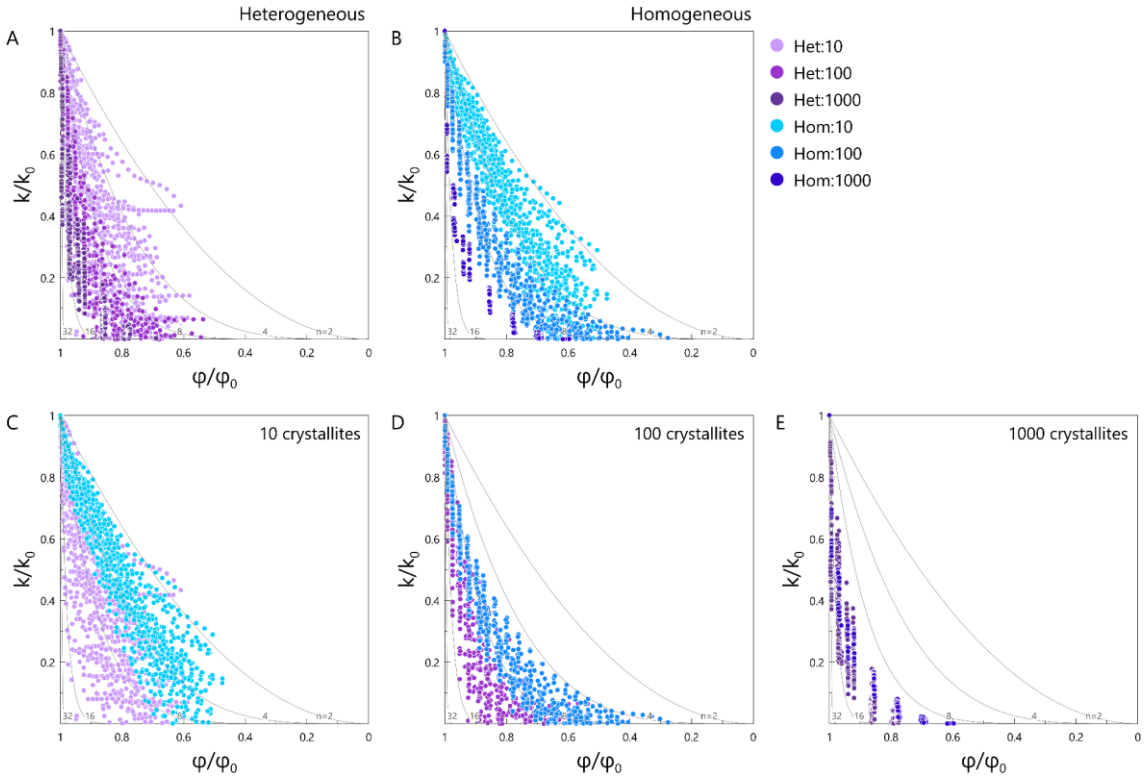

Figure 2: Variations in transport properties (expressed as normalized permeability-porosity relationship) of evolving two-dimensional porous geometries induced by mineral precipitation. Two structural classes, six different porous geometries, and three crystallization cases (10, 100, and 1000) are shown. Power-law bounds with different exponents (n = 2^x [x= 1,.., 5]) are also plotted. [top] (A) heterogeneous and (B) homogeneous and porous geometries. [bottom] Variance of decline in normalized permeability-porosity during stochastic growth of (C) 10, (D) 100, and (E) 1000 crystallites. Violet: heterogeneous and blue: homogenous cases.

Figures 3A-D and 3E-H compare the results for heterogeneous and homogeneous systems, respectively. Making a clear visual distinction between different geometries in each class (heterogeneous or homogeneous) is not possible (Figs. 3A and 3E). Figures 3B-C also show an indistinguishable data cloud for 10s and 10^2s. However, from Het_1 to Het_3, the scatter in the data points decreases, and the rate of permeability reduction increases. It might seem unexpected since Het_3 has more prominent flow pathways and higher initial permeability. Het_3's initial permeability is one order of magnitude higher than Het_1. Precipitation-included morphology alteration caused greater permeability impairment in Het_3 with a similar number of crystals. Het_3 porous geometry features massive highway (compared to others), meaning that small patches of solid precipitation can break down these fluid pathways into several smaller and less transmissive channels. One might therefore conclude that heterogeneous reservoir rocks are prone to more severe permeability impairment. For instance, fracture permeability can drop significantly and quickly, even with a tiny amount of mineral precipitation. This suggests that the initial state of the porous geometry plays a critical role in the extent of permeability impairment caused by mineral precipitation.

Although Hom_1 and Hom_2 geometries are different and represent ordered and disordered distributions of circular elements, their corresponding changes in permeability are approximately similar (Figs. 3E-H). It implies that studying geometry alteration in 2D microfluidic systems with similar ordered and disordered disks in Figure 1 may lead to similar outcomes regarding permeability evolution. Furthermore, the permeability reduction rate for Hom_3 geometry is less severe than in the other two homogeneous cases (Fig. 3G-H). Lower initial permeability, poor sorting of grains (two-size disks), and breakdown of pores by the distribution of smaller grains portray the initial state of pore morphologies. It is featured by a lower relative percentage of deterioration compared to Hom_1 and Hom_2.

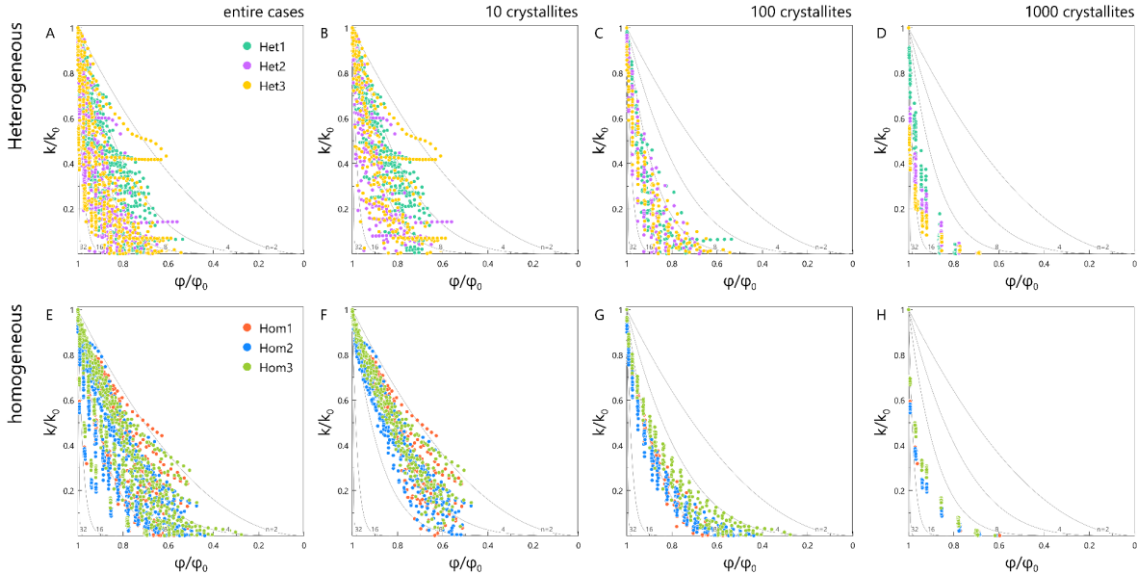

Figure 3: Variations in transport properties (expressed as normalized permeability-porosity relationship) of evolving two-dimensional porous geometries induced by mineral precipitation. Two structural classes, six different porous geometries, and three crystallization cases (10, 100, and 1000) are shown. Power-law bounds with different exponents ($n = 2^x$ [x= 1,.., 5]) are also plotted**.** [top row] Variations in heterogeneous geometries (A) entire crystallization cases, (B) 10, (C) 100, and (D) 1000 crystallites; [bottom row] Variations in homogenous geometries for (E) entire crystallization cases, (F) 10, (G) 100, and (H) 1000 crystallites.

It should be noted that the observed variations in permeability trendlines are also associated with the characteristics of 2D or pseduo2D systems (e.g., flow between sedimentary lamina or in fractures). For instance, in the heterogeneous geometries (Fig. 1), a handful of pore-throat locations control the overall flow and transport. In other words, there are few flow highways (the most transmissive flow paths) within the system, blocking which results in significant permeability decline. As such, when the system is heterogeneous and anisotropic, some sharp feedback (permeability decline) can be expected with minor changes in the system (porosity alteration). The severity of permeability decline and degree of variations is expected to be lower for three-dimensional porous geometries, particularly for a limited number of growing crystals. When there are fewer crystallites, the differences between realizations are more significant, implying that more spatially distributed nucleation is likely to smooth out the variations in permeability evolution.

Figures 4 and 5 show flow velocity maps, mineral precipitation patterns, and directional permeability values (k_x and k_y), and thus provide more detailed information regarding the spatial (pore volume change) and temporal evolution in the heterogeneous (Het_1) and homogeneous (Hom_1) systems, respectively. The x-axis shows the number of steps, and the y-axis shows the number of crystallites. Blue represents the grains, and white represents the precipitants. Two different probabilistic realizations, giving maximum and minimum permeability decline, are shown to demonstrate the effect of the spatial distribution of crystals. For example, subfigures E and F are two realizations with different spatial distributions of 100 crystallites. We aim to compare the realization in two instances: (a) at t= 2.35 x10^5 steps (A, B, C, and D) and (b) at ϕ/ϕ_0=0.9 (diagonal).

The spatial distribution of the mineral precipitates governs the degree of directional permeability loss. For example, in Figure 4G, the permeability impairment in the x direction is twice the y direction, but in Figure 4H it is the other way around. Since there is no (or very low) anisotropy for the homogeneous geometries, the difference between k_x and k_y for Hom_1 (Fig. 5) is lower than Het_1 (Fig. 4).

It is shown that the increasing number of growing crystals significantly contributes to a faster decline in permeability in temporal domains (Figs. 3). The precipitation maps and directional flow velocity profiles also illustrate how for the same porosity loss (ϕ/ϕ_0=0.9), a higher number of crystals can lead to a larger permeability decline. With a larger number of crystals, it is more likely to clog flow pathways earlier and thus with less precipitation. In contrast, fewer crystallites requires that the crystallites grow to sufficiently large size to block flow pathways. Additionally, with similar growth dynamics, the corresponding ξ for 10, 10^2, and 10^3 crystallites to reach the same porosity reduction are 2.40 x10^6, 6.00 x10^5, and 2.35 x10^5, respectively.

The effect of initial crystallites density on permeability evolution is also evident in the comparison at a given time (e.g., 2.35x10^5 steps) when individual crystals have similar sizes. In Figure 4D, 10 growing crystals occupied around 0.2% of the pore volume resulting in 1.5% and 6.9% permeability reduction in the x and y directions, respectively. As is illustrated in Figure 4, at a similar reaction progress (2.35x10^5 steps), a porosity changes of ϕ/ϕ_0=0.986 and 0.9 were observed for the 100 and 1000 crystallite cases, respectively, causing an average of 24% and 80% permeability decline (99% in the worst-case scenario, Fig. 4B).

The clustering and spread of initial crystals can also affect permeability in different directions. For example, Figures 4G-H represent two different distributions of 10 crystallites at the same step. For the case shown in Figure 4G, the permeability reduction ratio in the y direction is smaller than that in the x direction (k/k_0y=0.48 > k/k_0x=0.248). This is because the crystals to the left are clustered along the same highway in the y direction but spread out along different highways in the x direction, and growth that blocks several highways in the x direction only blocks a few in the y direction. In contrast, in the case depicted by Figure 4H, the crystals are spread along the same highways in the x direction, resulting in greater permeability reduction in the y direction. Similar behavior can be observed in homogeneous cases (see Figure 5H as an example), but the difference in permeability ratio values is less pronounced.

Overall, as the system evolves and porosity decreases, the difference between permeability values across increases (Figs. 2-3). There was limited variation between permeability values across different stochastic realizations in early times. For a higher number of crystals, the size of individual crystals is small at early times, so they cause limited and similar levels of permeability impairment. However, as the precipitates aggregate or become big enough to block a highway, their distribution can make more significant differences. Conversely, the mass is divided between fewer crystals for heterogeneous systems with fewer crystals. Therefore, based on their distribution, they can cause a considerable or minimal permeability reduction, and the standard deviation in permeability values is considerable from the beginning for these cases.

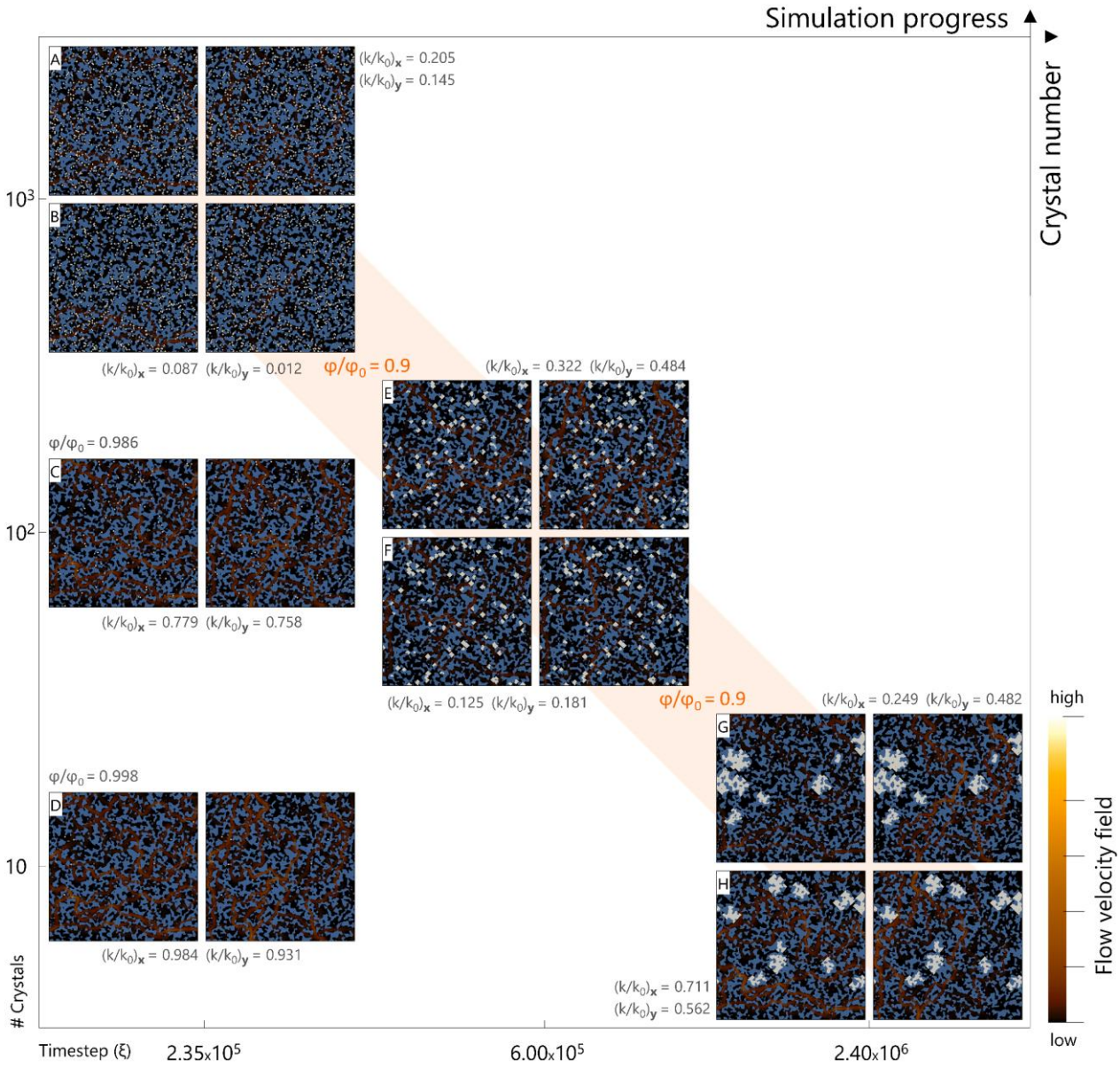

Figure 4: Pore morphology alterations because of mineral precipitation and growth for pseudo-rock geometries (heterogeneous 1 media in Figure 1). Besides the 2D surface growth stochastic realizations, normalized porosity loss (φ/φ_0), normalized permeability decline (k/k_0) in x,y-directions, and flow velocity fields are indicated as a function of crystallites number and simulation progress. For each part, the velocity map to the left and right represent the x and the y directions, respectively. The geometries on the diagonal have similar normalized porosity loss (φ/φ_0 = 0.9). (A) 1000 crystals - minimum permeability decline. (B) 1000 crystals - maximum permeability decline. (C) and (D) 100 and 10 crystals, respectively, at the same timestep as A and B. (E) Continuation of C - 100 crystals, minimum permeability decline. (F) 100 crystals - maximum permeability decline. (G) Continuation of D - 10 crystals, minimum permeability decline. (H) 10 crystals - maximum permeability decline.

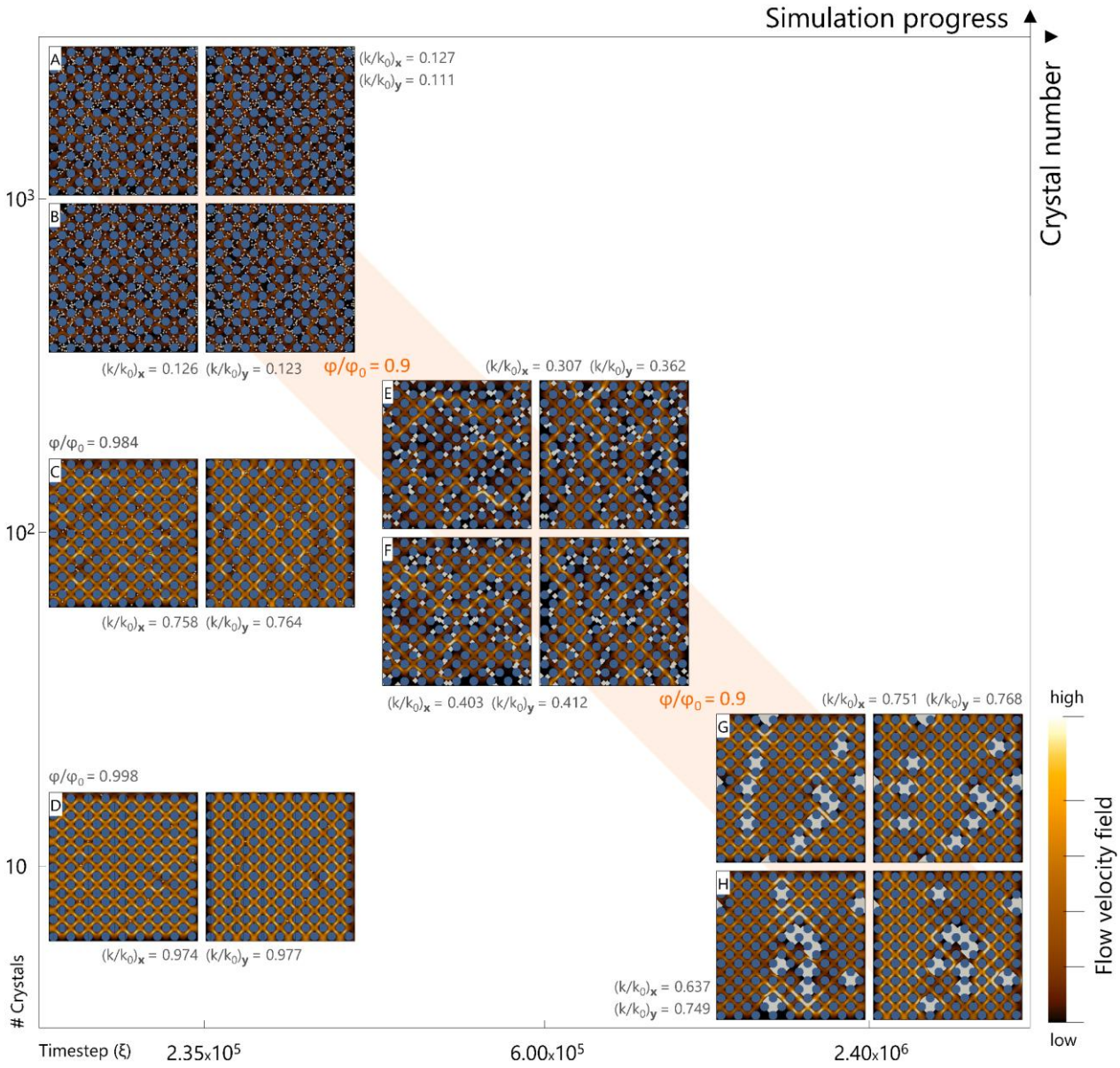

Figure 5: Pore morphology alterations as a result of mineral precipitation and growth for simplified geometries (homogeneous 1 media in Figure 1). Besides the 2D surface growth stochastic realizations, normalized porosity loss (φ/φ_0), normalized permeability decline (k/k_0) in x,y-directions, and flow velocity fields are indicated as a function of crystallites number and simulation progress. For each part, the velocity map to the left and right represent the x and the y directions, respectively. The geometries on the diagonal have similar normalized porosity loss (φ/φ_0 = 0.9). (A) 1000 crystals - minimum permeability decline. (B) 1000 crystals - maximum permeability decline. (C) and (D) 100 and 10 crystals, respectively, at the same timestep as A and B. (E) Continuation of C - 100 crystals, minimum permeability decline. (F) 100 crystals - maximum permeability decline. (G) Continuation of D - 10 crystals, minimum permeability decline. (H) 10 crystals - maximum permeability decline.

The total precipitated mass for a given porosity ratio is the same in all systems. It means that the size of each individual crystal will be smaller as the number of crystals increases because the mass is divided between more crystals. Therefore, at a given porosity ratio, 10 crystallite scenarios (10C) imply bigger crystals than 100C, and 100C than 1000C. However, in Figure 3, as a function of reaction progress, the size of crystals is similar as they grow at the same rate.

4 Upscaling

The common practice of accounting for effects of precipitation reactions on flow and transport is to use simplified permeability-porosity relations. Empirical, experimental, or theoretical models such as the Kozeny-Carman [57,58], Verma-Pruess [59,60], and power law (Table S2) are frequently used because of their convenience and simplicity, and their implementation in most of the commercial or open-access simulators for a wide range of geo-energy and geo-environmental applications.

In the models summarized in Table S2, *n* is a tuning parameter informed by experimental data or derived from smaller-scale simulations or the literature. For large-scale simulations, a medium-specific value of *n* is assigned to each grid cell based on the property map of the domain (for instance, rock type).

The power value *n* has a wide range of reported values[8] and can be correlated to factors such as mineralogy, clay fractions, clay surface area, pore size distribution, heterogeneity of the pore structure, and transport regime. A fixed value of n may not be an appropriate choice for describing the permeability-porosity changes [8]. The predictivity of permeability–porosity relations become more questionable when we deal with natural rocks with different minerals (varying kinetics) under different flow and transport conditions. Additionally, as shown by our pore-scale simulations, even with the same process and the same type of initial geometry, identical porosity changes might cause different changes in permeability. Put another way, the spatial distribution of the deposited solid plays an essential role in changing the hydrodynamics of porous media. Therefore, it is almost impossible to be able to capture the permeability-porosity evolution with a single clogging model.

On the other hand, incorporating too many complexities into a clogging model is impractical, inefficient, and one might even argue to be unnecessary. In particular, when dealing with systems with millions of grid cells.

As an effort to address this dual challenge, we propose a hierarchical upscaling approach which considers complexity while allowing to use of readily available and practical formulations. The novelty of our approach is to upscale permeability–porosity evolution together with the uncertainties around them, with a special focus on permeability changes due to mineral precipitation.

The power law relations have been typically used to describe the effects of mineral precipitation for various pore morphology-altering processes such as biomass accumulation, dissolution, and precipitation. According to Hommel et al.,[7] modified permeability–porosity relations that are more complex do not necessarily provide fundamentally different predictions than simple power-law equations with a proper exponent. Because many of these more complex relations already contain a power-law term or have similar behavior. Furthermore, the simplicity and inclusiveness of the power-law equation make it suitable for implementation in many flow simulations and RTM tools. Therefore, we fit a power law curve for each realization (each trendline in Fig. S2) and extract the coefficient *n*.

The distribution of *n* values is shown in Figure 8 and in supplemental Figures S4 to S7. In Figure 8, we compared the distributions of n values for all the heterogeneous cases (A) and all the homogeneous cases (B and C). The heterogeneous cases showed a broader distribution of power law parameter than homogeneous cases. In Figure 8.A, the values of power law parameter that are distributed from 75 to 150 are related to Het_3, 1000 crystallites case. This case shows the sharpest

decline in permeability. Other heterogeneous cases overlap, and their behavior is not distinguishable. In contrast, the homogeneous cases exhibited more ordered behavior, as shown in Figure 8.B. The results for each individual case (Fig. S4), each structure (Fig. S5), each number of crystallites (Fig. S6), and all the cases together (Fig. S7) provides a better understanding of the clogging behavior of the simulated cases.

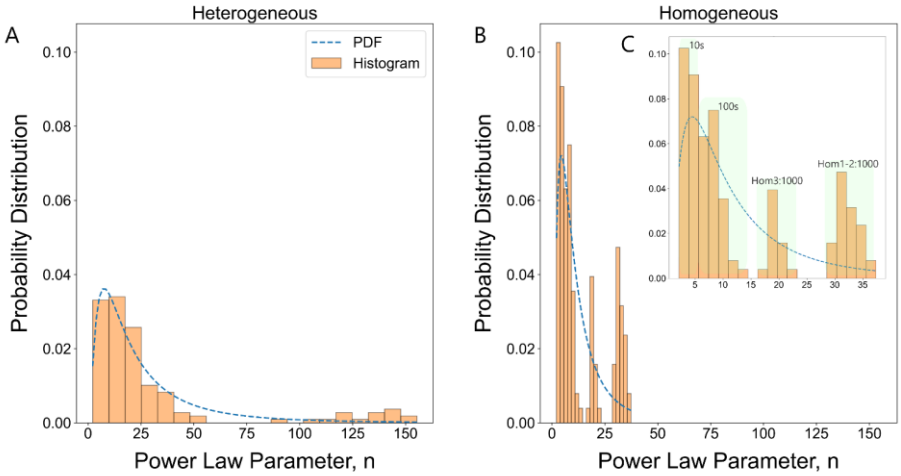

Figure 6: Probability distribution function (PDF) and statistical variance of power-law exponent (*n*) for two structural classes and six different porous geometries as a function of crystallization cases (10, 100, and 1000).

The suggested upscaling framework for stepwise increasing of the grid size is illustrated in Figure 9. To enable broader applications in different precipitation processes, in the summary here, the number of secondary crystallites and their spatial distribution was considered to follows a probabilistic distribution at the scale of interest, as previously discussed in our probabilistic nucleation and growth model [9,22,39–42]. The framework works as follows:

A. Pore-scale modeling: The procedure begins with pore-scale modeling, which involves performing a Monte Carlo type of simulation to capture the clogging behavior of a given system. The probabilistic nucleation model (based on the classical nucleation theory (CNT)) determines the spatial distribution and the number of crystallites. This enables accounting for the effects of parameters such as temperature, supersaturation, and interfacial free energy on the number of crystallites and crystal growth rate.
B. Deriving the distribution of the clogging model parameter: The permeability should be calculated at several stages points during the evolution of the system in step A. Next, by fitting the preferred clogging model curve (we used power law in this paper) to each simulation, a distribution of the clogging model parameter can be derived, which is likely to be a (log)normal distribution as more data is acquired. This step provides a probability distribution function (PDF) that will be used in the next step.
C. Continuum-scale simulations: small-scale continuum simulations should be performed using the simple and convenient clogging model to update the permeability. But rather than a fixed exponent, each grid cell samples a random power law parameter, n, from the PDF derived in step B. The random number generator for sampling the power law parameter works based on the

generated PDF. This step can be replaced using a proxy model or Monte Carlo to reduce the number of simulations.

D. Deriving a new distribution of the clogging model parameter, n: The permeability of the whole domain should be calculated at several points during the simulation time using a proper averaging technique. The permeability and porosity values will represent a new PDF for the clogging model parameter.
E. Steps C-D can optionally be repeated until the distribution reaches stability or until a particular stopping criterion is met, such as reaching the grid size of the application-scale simulation. At this point, the final PDF for the clogging model parameter is generated and will be used for the numerical simulations of the reactive system. In majority of RTM purposes, a three-step scheme should be sufficient to reflect the pore scale probabilistic dynamics to fit-for-purpose application scale. For instance, consider a 500*500 grid simulation at pore scale (similar to present study), the micrometer-scale grid size represents an entire domain of millimeter-scale. At continuum scale (core-scale in some application), the mm-scale grid size constitutes centimeters to meters scale domain. In the application-scale step, then grid size of several meters covers the whole kilometer-scale domain (Fig. S8).

By following this framework, the complexities of permeability changes in porous media can be represented at different scales while ensuring the readiness of implementation. Additionally, the gradual transition from a small to a larger scale helps to capture the interactions between the consecutive scales and ensures a better representation of system behaviors.

As we mentioned in our previous publications [40,42,55], in some specific systems, the probability of nucleation occurring in a particular area and at a specific time is exceptionally high, enabling the employment of deterministic approaches to handle the nucleation process, which significantly simplifies the analysis and modeling.

The proposed framework can be applied to any two- and three-dimensional system. The pore-scale insights can be from high-resolution imaging or simulations. The CPU time of the method should be evaluated due to the computational cost of performing Monte Carlo-type stochastic realizations. Including these larger structural scales is out of the scope of this work but is a target of future research.

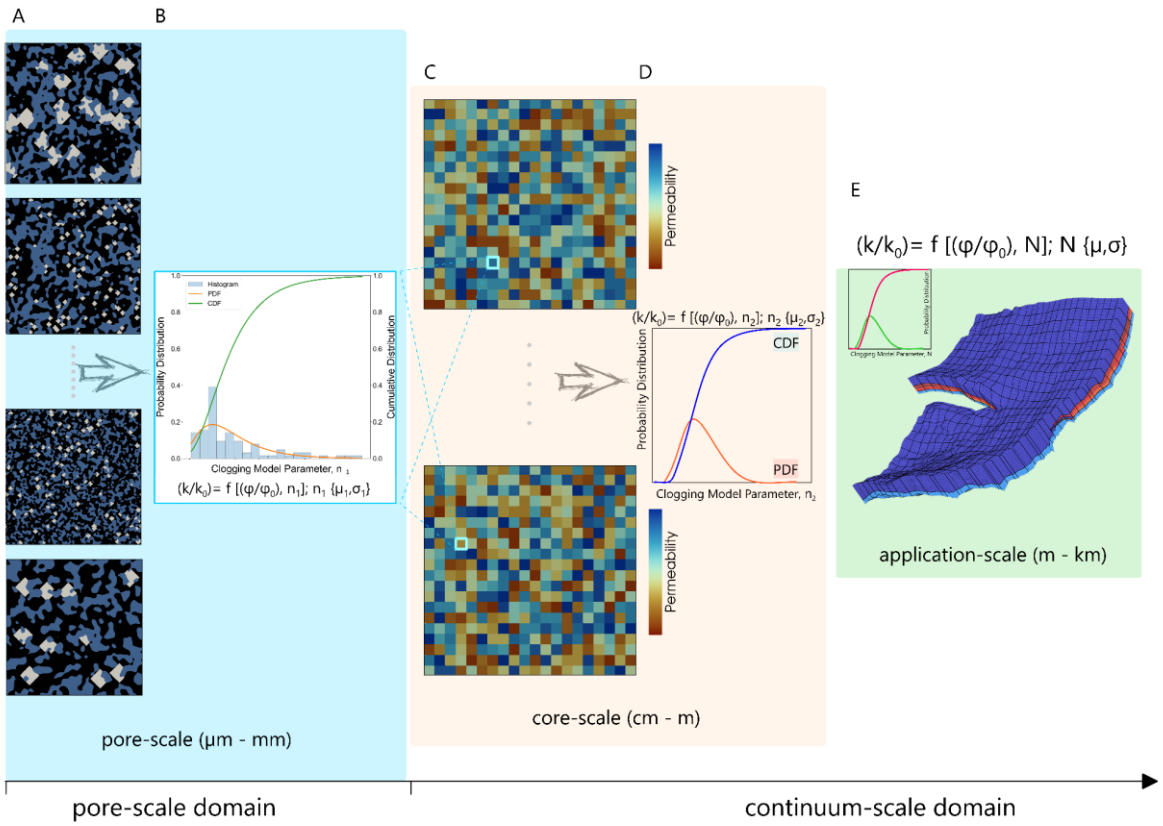

Figure 7: Proposed scheme for upscaling variations in permeability-porosity induced by mineral precipitation and porous media alteration for reactive systems.

5 Conclusions

In this study, we took a statistical approach to investigate the effect of crystallite distribution on the co-evolution of permeability-porosity due to mineral precipitation. We also introduced an upscaling approach for the variations in permeability changes with implications for clean water and sanitation, climate action, and affordable and clean energy. The following points summarize the major findings of our work:

- The spatial distribution of the mineral precipitates and the initial state of the porous geometry play critical roles in changing the hydrodynamics of porous media. Therefore, even with the same process and the same porous morphology, identical porosity changes during mineral precipitation might cause different changes in permeability. Capturing the permeability-porosity evolution with a single clogging model might result in considerable uncertainties.
- Anisotropic and Heterogeneous reservoir rocks are prone to more severe permeability impairment, as minor changes in porosity can lead to severe permeability impairments.
- Fitting the power-law function to each realization resulted in a wide range of power-law coefficient *n*. For most realizations, a (log)normal distribution is obtained. The higher the number of crystallites, the permeability–porosity data is less scattered.
- Distribution of the deposited crystallites (controlled by mineral nucleation) adds an extra level of complexity to the mineral precipitation process, which should be taken into consideration in continuum-scale reactive transport simulations. To address this issue, we proposed a hierarchical upscaling approach.

Acknowledgments

This publication has been produced with support from the projects "clean offshore energy by hydrogen storage in petroleum reservoirs" (funded by Research Council of Norway under grant number 315804) and "solid and salt precipitation kinetics during CO2 injection into reservoir" (funded by Norway Grants under grant number UMO-2019/34/H/ST10/00564 through the GRIEG Program). The high-performance computing was carried out on the Norwegian Research and Education Cloud (NREC), provided by the University of Bergen and the University of Oslo.

Open Research

The simulation results supporting the research presented in this paper are openly available at the Dataverse repository at doi: https://doi.org/10.18710/3LT3QU (Masoudi et al., 2023). The Python script to implement the probabilistic nucleation model into reactive transport models (RTM) is accessible at https://doi.org/10.1038/s41598-021-95237-7 (Nooraiepour et al., 2021) (https://static-content.springer.com/esm/art%3A10.1038%2Fs41598-021-95237-7/MediaObjects/41598_2021_95237_MOESM1_ESM.pdf). The reactive probailistic LBM code are available to research scientist from the authors upon reasonable request. The open-access Yantra LBM tool is also used in this study https://doi.org/10.1016/j.pce.2014.03.001 (Patel et al., 2014).

References

(1) Battiato, I.; Ferrero V, P. T.; O' Malley, D.; Miller, C. T.; Takhar, P. S.; Valdés-Parada, F. J.; Wood, B. D. Theory and Applications of Macroscale Models in Porous Media. *Transp. Porous Media* **2019**, *130* (1), 5–76. https://doi.org/10.1007/s11242-019-01282-2.

(2) Menke, H. P.; Maes, J.; Geiger, S. Upscaling the Porosity–Permeability Relationship of a Microporous Carbonate for Darcy-Scale Flow with Machine Learning. *Sci. Rep.* **2021**, *11* (1), 2625. https://doi.org/10.1038/s41598-021-82029-2.

(3) Dvorkin, J.; Derzhi, N. Rules of Upscaling for Rock Physics Transforms: Composites of Randomly and Independently Drawn Elements. *GEOPHYSICS* **2012**, *77* (3), WA129–WA139. https://doi.org/10.1190/geo2011-0268.1.

(4) Zhang, X.; Ma, F.; Yin, S.; Wallace, C. D.; Soltanian, M. R.; Dai, Z.; Ritzi, R. W.; Ma, Z.; Zhan, C.; Lü, X. Application of Upscaling Methods for Fluid Flow and Mass Transport in Multi-Scale Heterogeneous Media: A Critical Review. *Appl. Energy* **2021**, *303*, 117603. https://doi.org/https://doi.org/10.1016/j.apenergy.2021.117603.

(5) Soleymanzadeh, A.; Parvin, S.; Kord, S. Effect of Overburden Pressure on Determination of Reservoir Rock Types Using RQI/FZI, FZI* and Winland Methods in Carbonate Rocks. *Pet. Sci.* **2019**, *16* (6), 1403–1416. https://doi.org/10.1007/s12182-019-0332-8.

(6) Li, J.; Hussaini, S. R.; Dvorkin, J. Permeability-Porosity Relations from Single Image of Natural Rock: Subsampling Approach. *J. Pet. Sci. Eng.* **2020**, *194*, 107541. https://doi.org/https://doi.org/10.1016/j.petrol.2020.107541.

(7) Hommel, J.; Coltman, E.; Class, H. Porosity–Permeability Relations for Evolving Pore Space: A Review with a Focus on (Bio-)Geochemically Altered Porous Media. *Transp. Porous Media* **2018**, *124* (2), 589–629. https://doi.org/10.1007/s11242-018-1086-2.

(8) Seigneur, N.; Mayer, K. U.; Steefel, C. I. Reactive Transport in Evolving Porous Media. *Rev. Mineral. Geochemistry* **2019**, *85* (1), 197–238. https://doi.org/10.2138/rmg.2019.85.7.

(9) Masoudi, M.; Fazeli, H.; Miri, R.; Hellevang, H. Pore Scale Modeling and Evaluation of Clogging Behavior of Salt Crystal Aggregates in CO2-Rich Phase during Carbon Storage. *Int. J. Greenh. Gas Control* **2021**, *111*, 103475. https://doi.org/https://doi.org/10.1016/j.ijggc.2021.103475.

(10) Poonoosamy, J.; Wanner, C.; Alt Epping, P.; Águila, J. F.; Samper, J.; Montenegro, L.; Xie, M.; Su, D.; Mayer, K. U.; Mäder, U.; Van Loon, L. R.; Kosakowski, G. Benchmarking of Reactive Transport Codes for 2D Simulations with Mineral Dissolution–Precipitation Reactions and Feedback on Transport Parameters. *Comput. Geosci.* **2021**, *25* (4), 1337–1358. https://doi.org/10.1007/s10596-018-9793-x.

(11) Kang, Q.; Chen, L.; Valocchi, A. J.; Viswanathan, H. S. Pore-Scale Study of Dissolution-Induced Changes in Permeability and Porosity of Porous Media. *J. Hydrol.* **2014**, *517*, 1049–1055. https://doi.org/10.1016/j.jhydrol.2014.06.045.

(12) Prasianakis, N. I.; Gatschet, M.; Abbasi, A.; Churakov, S. V. Upscaling Strategies of Porosity-Permeability Correlations in Reacting Environments from Pore-Scale Simulations. *Geofluids* **2018**, *2018*, 9260603. https://doi.org/10.1155/2018/9260603.

(13) Dashtian, H.; Bakhshian, S.; Hajirezaie, S.; Nicot, J. P.; Hosseini, S. A. Convection-Diffusion-Reaction of CO 2 -Enriched Brine in Porous Media: A Pore-Scale Study. *Comput. Geosci.* **2019**, *125*, 19–29. https://doi.org/10.1016/j.cageo.2019.01.009.

(14) Noiriel, C.; Daval, D. Pore-Scale Geochemical Reactivity Associated with CO2 Storage: New Frontiers at the Fluid–Solid Interface. *Acc. Chem. Res.* **2017**, *50* (4), 759–768. https://doi.org/10.1021/acs.accounts.7b00019.

(15) Menke, H. P.; Bijeljic, B.; Andrew, M. G.; Blunt, M. J. Dynamic Three-Dimensional Pore-Scale Imaging of Reaction in a Carbonate at Reservoir Conditions. *Environ. Sci. Technol.* **2015**, *49* (7), 4407–4414. https://doi.org/10.1021/es505789f.

(16) Noiriel, C.; Soulaine, C. Pore-Scale Imaging and Modelling of Reactive Flow in Evolving Porous Media: Tracking the Dynamics of the Fluid–Rock Interface. *Transp. Porous Media* **2021**, *140* (1), 181–213. https://doi.org/10.1007/s11242-021-01613-2.

(17) Fazeli, H.; Nooraiepour, M.; Hellevang, H. Microfluidic Study of Fracture Dissolution in Carbonate-Rich Caprocks Subjected to CO2-Charged Brine. *Ind. Eng. Chem. Res.* **2020**, *59* (1). https://doi.org/10.1021/acs.iecr.9b06048.

(18) Hassanpouryouzband, A.; Joonaki, E.; Vasheghani Farahani, M.; Takeya, S.; Ruppel, C.; Yang, J.; English, N. J.; Schicks, J. M.; Edlmann, K.; Mehrabian, H.; Aman, Z. M.; Tohidi, B. Gas Hydrates in Sustainable Chemistry. *Chem. Soc. Rev.* **2020**, *49* (15), 5225–5309. https://doi.org/10.1039/C8CS00989A.

(19) Masoudi, M.; Miri, R.; Hellevang, H.; Kord, S. Modified PC-SAFT Characterization Technique for Modeling Asphaltenic Crude Oil Phase Behavior. *Fluid Phase Equilib.* **2020**, *513*, 112545. https://doi.org/https://doi.org/10.1016/j.fluid.2020.112545.

(20) Daryasafar, A.; Masoudi, M.; Kord, S.; Madani, M. Evaluation of Different Thermodynamic Models in Predicting Asphaltene Precipitation: A Comparative Study. *Fluid Phase Equilib.* **2020**, *514*, 112557. https://doi.org/https://doi.org/10.1016/j.fluid.2020.112557.

(21) Nooraiepour, M.; Fazeli, H.; Miri, R.; Hellevang, H. Salt Precipitation during Injection of CO2 into Saline Aquifers: Lab-on-Chip Experiments on Glass and Geomaterial Microfluidic Specimens. *SSRN* **2019**. https://doi.org/10.2139/ssrn.3365553.

(22) Fazeli, H.; Masoudi, M.; Patel, R. A.; Aagaard, P.; Hellevang, H. Pore-Scale Modeling of Nucleation and Growth in Porous Media. *ACS Earth Sp. Chem.* **2020**, *4* (2), 249–260. https://doi.org/10.1021/acsearthspacechem.9b00290.

(23) Nooraiepour, M.; Fazeli, H.; Miri, R.; Hellevang, H. Effect of CO2 Phase States and Flow Rate on Salt Precipitation in Shale Caprocks - A Microfluidic Study. *Environ. Sci. Technol.* **2018**, *52* (10), 6050–6060. https://doi.org/10.1021/acs.est.8b00251.

(24) Miri, R.; van Noort, R.; Aagaard, P.; Hellevang, H. New Insights on the Physics of Salt Precipitation during Injection of CO2 into Saline Aquifers. *INT J GREENH GAS CON* **2015**, *43*, 10–21. https://doi.org/10.1016/j.ijggc.2015.10.004.

(25) Renard, F.; Putnis, C. V.; Montes-Hernandez, G.; Ruiz-Agudo, E.; Hovelmann, J.; Sarret, G. Interactions of Arsenic with Calcite Surfaces Revealed by in Situ Nanoscale Imaging. *Geochim. Cosmochim. Acta* **2015**, *159*, 61–79. https://doi.org/10.1016/j.gca.2015.03.025.

(26) Putnis, C. V; Renard, F.; King, H. E.; Montes-Hernandez, G.; Ruiz-Agudo, E. Sequestration of Selenium on Calcite Surfaces Revealed by Nanoscale Imaging. *Environ. Sci. Technol.* **2013**, *47* (23), 13469–13476. https://doi.org/10.1021/es403637u.

(27) Renard, F.; Putnis, C. V; Montes-Hernandez, G.; King, H. E.; Breedveld, G. D.; Okkenhaug, G. Sequestration of Antimony on Calcite Observed by Time-Resolved Nanoscale Imaging. *Environ. Sci. Technol.* **2018**, *52*

(1), 107–113. https://doi.org/10.1021/acs.est.7b04727.
(28) Guren, M. G.; Putnis, C. V; Montes-Hernandez, G.; King, H. E.; Renard, F. Direct Imaging of Coupled Dissolution-Precipitation and Growth Processes on Calcite Exposed to Chromium-Rich Fluids. *Chem. Geol.* **2020**, *552*, 119770. https://doi.org/https://doi.org/10.1016/j.chemgeo.2020.119770.
(29) Julia, M.; Putnis, C. V; King, H. E.; Renard, F. Coupled Dissolution-Precipitation and Growth Processes on Calcite, Aragonite, and Carrara Marble Exposed to Cadmium-Rich Aqueous Solutions. *Chem. Geol.* **2023**, *621*, 121364. https://doi.org/https://doi.org/10.1016/j.chemgeo.2023.121364.
(30) Zhang, T.; Gregory, K.; Hammack, R. W.; Vidic, R. D. Co-Precipitation of Radium with Barium and Strontium Sulfate and Its Impact on the Fate of Radium during Treatment of Produced Water from Unconventional Gas Extraction. *Environ. Sci. Technol.* **2014**, *48* (8), 4596–4603. https://doi.org/10.1021/es405168b.
(31) Poonoosamy, J.; Haber-Pohlmeier, S.; Deng, H.; Deissmann, G.; Klinkenberg, M.; Gizatullin, B.; Stapf, S.; Brandt, F.; Bosbach, D.; Pohlmeier, A. Combination of MRI and SEM to Assess Changes in the Chemical Properties and Permeability of Porous Media Due to Barite Precipitation. *Minerals*. 2020. https://doi.org/10.3390/min10030226.
(32) Poonoosamy, J.; Klinkenberg, M.; Deissmann, G.; Brandt, F.; Bosbach, D.; Mäder, U.; Kosakowski, G. Effects of Solution Supersaturation on Barite Precipitation in Porous Media and Consequences on Permeability: Experiments and Modelling. *Geochim. Cosmochim. Acta* **2020**, *270*, 43–60. https://doi.org/https://doi.org/10.1016/j.gca.2019.11.018.
(33) Deng, H.; Navarre-Sitchler, A.; Heil, E.; Peters, C. Addressing Water and Energy Challenges with Reactive Transport Modeling. *Environ. Eng. Sci.* **2021**, *38* (3), 109–114. https://doi.org/10.1089/ees.2021.0009.
(34) Tranter, M.; De Lucia, M.; Wolfgramm, M.; Kühn, M. Barite Scale Formation and Injectivity Loss Models for Geothermal Systems. *Water*. 2020. https://doi.org/10.3390/w12113078.
(35) Miri, R.; Hellevang, H. Salt Precipitation during CO2 Storage—A Review. *INT J GREENH GAS CON* **2016**, *51*, 136–147. https://doi.org/10.1016/j.ijggc.2016.05.015.
(36) Berntsen, A.; Todorovic, J.; Raphaug, M.; Torsæter, M.; Chavez Panduro, E. A.; Gawel, K. Salt Clogging during Supercritical CO2 Injection into a Downscaled Borehole Model. *Int. J. Greenh. Gas Control* **2019**, *86*, 201–210. https://doi.org/https://doi.org/10.1016/j.ijggc.2019.04.009.
(37) Pham, V. T. H.; Lu, P.; Aagaard, P.; Zhu, C.; Hellevang, H. On the Potential of CO2–Water–Rock Interactions for CO2 Storage Using a Modified Kinetic Model. *Int. J. Greenh. Gas Control* **2011**, *5* (4), 1002–1015. https://doi.org/https://doi.org/10.1016/j.ijggc.2010.12.002.
(38) Poonoosamy, J.; Westerwalbesloh, C.; Deissmann, G.; Mahrous, M.; Curti, E.; Churakov, S. V; Klinkenberg, M.; Kohlheyer, D.; von Lieres, E.; Bosbach, D.; Prasianakis, N. I. A Microfluidic Experiment and Pore Scale Modelling Diagnostics for Assessing Mineral Precipitation and Dissolution in Confined Spaces. *Chem. Geol.* **2019**, *528*, 119264. https://doi.org/https://doi.org/10.1016/j.chemgeo.2019.07.039.
(39) Masoudi, M. Near Wellbore Processes during Carbon Capture, Utilization, and Storage (CCUS): An Integrated Modeling Approach. **2021**.
(40) Nooraiepour, M.; Masoudi, M.; Shokri, N.; Hellevang, H. Probabilistic Nucleation and Crystal Growth in Porous Medium: New Insights from Calcium Carbonate Precipitation on Primary and Secondary Substrates. *ACS Omega* **2021**, *6* (42), 28072–28083. https://doi.org/10.1021/acsomega.1c04147.
(41) Deng, H.; Poonoosamy, J.; Molins, S. A Reactive Transport Modeling Perspective on the Dynamics of Interface-Coupled Dissolution-Precipitation. *Appl. Geochemistry* **2022**, *137*, 105207. https://doi.org/https://doi.org/10.1016/j.apgeochem.2022.105207.
(42) Nooraiepour, M.; Masoudi, M.; Hellevang, H. Probabilistic Nucleation Governs Time, Amount, and Location of Mineral Precipitation and Geometry Evolution in the Porous Medium. *Sci. Rep.* **2021**, *11* (1). https://doi.org/10.1038/s41598-021-95237-7.
(43) Masoudi, M.; Nooraiepour, M.; Hellevang, H. The Effect of Preferential Nucleation Sites on the Distribution of Secondary Mineral Precipitates. In *83rd EAGE Annual Conference & Exhibition*; European Association of Geoscientists & Engineers: Madrid, Spain, 2022; Vol. 2022, pp 1–5. https://doi.org/https://doi.org/10.3997/2214-4609.202210445.
(44) Ghezzehei, T. A. Linking Sub-Pore Scale Heterogeneity of Biological and Geochemical Deposits with Changes in Permeability. *Adv. Water Resour.* **2012**, *39*, 1–6. https://doi.org/https://doi.org/10.1016/j.advwatres.2011.12.015.
(45) Li, X.; Huang, H.; Meakin, P. Level Set Simulation of Coupled Advection-Diffusion and Pore Structure

Evolution Due to Mineral Precipitation in Porous Media. *Water Resour. Res.* **2008**, *44* (12). https://doi.org/https://doi.org/10.1029/2007WR006742.

(46) Ahkami, M.; Parmigiani, A.; Di Palma, P. R.; Saar, M. O.; Kong, X.-Z. A Lattice-Boltzmann Study of Permeability-Porosity Relationships and Mineral Precipitation Patterns in Fractured Porous Media. *Comput. Geosci.* **2020**, *24* (5), 1865–1882. https://doi.org/10.1007/s10596-019-09926-4.

(47) Yoon, H.; Major, J.; Dewers, T.; Eichhubl, P. Application of a Pore-Scale Reactive Transport Model to a Natural Analog for Reaction-Induced Pore Alterations. *J. Pet. Sci. Eng.* **2017**, *155*, 11–20. https://doi.org/https://doi.org/10.1016/j.petrol.2017.01.002.

(48) Beckingham, L. E. Evaluation of Macroscopic Porosity-Permeability Relationships in Heterogeneous Mineral Dissolution and Precipitation Scenarios. *Water Resour. Res.* **2017**, *53* (12), 10217–10230. https://doi.org/https://doi.org/10.1002/2017WR021306.

(49) Noiriel, C.; Seigneur, N.; Le Guern, P.; Lagneau, V. Geometry and Mineral Heterogeneity Controls on Precipitation in Fractures: An X-Ray Micro-Tomography and Reactive Transport Modeling Study. *Adv. Water Resour.* **2021**, *152*, 103916. https://doi.org/https://doi.org/10.1016/j.advwatres.2021.103916.

(50) Noiriel, C.; Steefel, C. I.; Yang, L.; Bernard, D. Effects of Pore-Scale Precipitation on Permeability and Flow. *Adv. Water Resour.* **2016**, *95*, 125–137. https://doi.org/https://doi.org/10.1016/j.advwatres.2015.11.013.

(51) Weinhardt, F.; Deng, J.; Hommel, J.; Vahid Dastjerdi, S.; Gerlach, R.; Steeb, H.; Class, H. Spatiotemporal Distribution of Precipitates and Mineral Phase Transition During Biomineralization Affect Porosity–Permeability Relationships. *Transp. Porous Media* **2022**, *143* (2), 527–549. https://doi.org/10.1007/s11242-022-01782-8.

(52) Parvin, S.; Masoudi, M.; Sundal, A.; Miri, R. Continuum Scale Modelling of Salt Precipitation in the Context of CO2 Storage in Saline Aquifers with MRST Compositional. *Int. J. Greenh. Gas Control* **2020**, *99*, 103075. https://doi.org/https://doi.org/10.1016/j.ijggc.2020.103075.

(53) Gostick, J. T.; Khan, Z. A.; Tranter, T. G.; Kok, M. D. R.; Agnaou, M.; Sadeghi, M.; Jervis, R. PoreSpy: A Python Toolkit for Quantitative Analysis of Porous Media Images. *J. Open Source Softw.* **2019**, *4* (37), 1296.

(54) Percolation. In *Physics of Flow in Porous Media*; Hansen, A., Flekkøy, E. G., Feder, J., Eds.; Cambridge University Press: Cambridge, 2022; pp 63–84. https://doi.org/DOI: 10.1017/9781009100717.005.

(55) Nooraiepour, M.; Masoudi, M.; Shorki, N.; Hellevang, H. Precipitation-Induced Geometry Evolution in Porous Media: Numerical and Experimental Insights Based on New Model on Probabilistic Nucleation and Mineral Growth. *SSRN Electron. J.* **2022**, No. October. https://doi.org/10.2139/ssrn.4272555.

(56) Patel, R. A. *Yantra*.

(57) Kozeny, J. Uber Kapillare Leitung Des Wassers Im Boden-Aufstieg, Versickerung Und Anwendung Auf Die Bewasserung, Sitzungsberichte Der Akademie Der Wissenschaften Wien. *Math. Naturwissenschaftliche Abteilung* **1927**, *136*, 271–306.

(58) Carman, P. C. Fluid Flow through Granular Beds. *Trans. Inst. Chem. Eng.* **1937**, *15*, 150–166.

(59) Verma, A.; Pruess, K. Thermohydrological Conditions and Silica Redistribution near High-Level Nuclear Wastes Emplaced in Saturated Geological Formations. *J. Geophys. Res.* **1988**, *93* (B2), 1159–1173.

(60) Pruess, K.; Müller, N. Formation Dry-out from CO2 Injection into Saline Aquifers: 1. Effects of Solids Precipitation and Their Mitigation. *Water Resour. Res.* **2009**, *45* (3), n/a-n/a. https://doi.org/10.1029/2008WR007101.